RSC Advances

PAPER

View Article Online
View Journal | View Issue

Cite this: *RSC Adv.*, 2021, **11**, 16034

Boosting charge separation and nitrogen vacancies in graphitic carbon nitride by implanted strontium vanadate for highly efficient photocatalytic reduction of hexavalent chromium

Yuzhi Zhou, Shi-Zhao Kang, Lixia Qin and Xiangqing Li *

Received 24th February 2021
Accepted 17th April 2021

DOI: 10.1039/d1ra01489g

rsc.li/rsc-advances

Strontium vanadate nanoparticles embedded graphitic carbon nitride (g-C_3N_4/$Sr_2V_2O_7$) was facilely prepared *in situ via* a hydrothermal method. It was shown that the $Sr_2V_2O_7$ nanoparticles implanted into g-carbon nitride had a small size and high distribution. Importantly, compared with some other photocatalysts, the as-prepared g-C_3N_4/$Sr_2V_2O_7$ nanohybrid showed excellent photocatalytic activity for reduction of Cr(VI), and as high as 99% efficiency for Cr(VI) reduction (100 mg L^{-1}) was reached within 8 min. Moreover, its activity was hardly changed after five cycles, demonstrating that the developed g-C_3N_4/$Sr_2V_2O_7$ nanohybrid was highly stable and promising an efficacious disposal of Cr(VI) in water. It was confirmed that the improved charge separation owing to more nitrogen vacancies in the hybrid was the main reason for the improved performance of the g-C_3N_4-$Sr_2V_2O_7$ nanohybrid.

Introduction

Nowadays, heavy metal ions in water have received extensive attention because of their serious harm to human and animal health. Among these ions, Cr(VI) is one of the most commonly found toxic ions in wastewater,[1] which seriously threatens ecological systems and could cause great damage to human health and induce many diseases such as cancer, dermatitis, liver damage, and inherited gene deficiency.[2] Therefore, eliminating Cr(VI) from aquatic environments has drawn much attention all around the world.

In those technologies for Cr(VI) removal,[3] photocatalytic technology plays a dominant role in solving the problem of environmental pollution because of its simple operation that is clean, and has high repeatability.[4] As a significant organic semiconductor photocatalyst, g-C_3N_4 has been widely used in H_2 evolution,[5] pollutants degradation,[6] CO_2 reduction,[7] and other fields due to its facile preparation, nontoxicity, excellent electronic properties. Nevertheless, the photocatalytic activity of single g-C_3N_4 is generally undesirable as a result of fast e^-/h^+ recombination.[8]

Several strategies have been developed to facilitate separation and transfer of photoinduced charges, such as doping, coupling with other semiconductors.[9] For instance, 95% of Cr(VI) can be removed by porous (P,Mo)-g-C_3N_4 prepared using a polycondensation strategy under sunlight irradiation for 120 min.[10] A phosphorus-doped g-C_3N_4/SnS synthesized *via* hydrothermal method can completely remove 100 mg L^{-1} Cr(VI) after irradiation for 60 min.[11] However, tedious synthetic process[12] or quick photocorrosion of some metal sulfides restricts their application in Cr(VI) removal. Moreover, the stability of some common photocatalysts and the degradation rate towards Cr(VI) are still unsatisfying. Therefore, it is highly challenging to develop effective and reusable g-C_3N_4-based materials for photocatalytic reduction of Cr(VI).

Metal vanadates possessing high thermal stability have received significant interest due to their potential application in chemical sensors, transparent conductors and photocatalysts.[13] As one of the important vanadates, strontium vanadate is widely used in the field of white-light-emitting devices and microwave-dielectrics.[14] While there is few application in photocatalysis. Interestingly, the result of electronic structure calculation confirms that the valence band of $Sr_2V_2O_7$ is mostly supported by oxygen atoms, and the bottom of the conduction band is mostly composed of the d orbitals of vanadium atoms.[14] And the 3d orbital of vanadium is generally situated below the analogous d orbitals of some transition metals, and the bottom of conduction band is decreased.[15] Therefore, $Sr_2V_2O_7$ could be an excellent candidate for e^-/h^+ separation if a heterojunction system composed of g-C_3N_4 and $Sr_2V_2O_7$ was smartly constructed in that it would greatly boost the charge transmission.

Herein, by hydrothermal method, small sized $Sr_2V_2O_7$ is evenly *in situ* incorporated in g-C_3N_4. The as-prepared g-C_3N_4/$Sr_2V_2O_7$ nanohybrid is characterized, and its performance is evaluated by photocatalytic reduction of Cr(VI). Moreover, the durability and stability of the g-C_3N_4/$Sr_2V_2O_7$ hybrid are examined by consecutive cycling experiment. The research could pave a new way for fabricating highly active and reusable semiconductor photocatalysts for the removal of heavy metal ions in wastewater.

Shanghai Institute of Technology, China. E-mail: xqli@sit.edu.cn

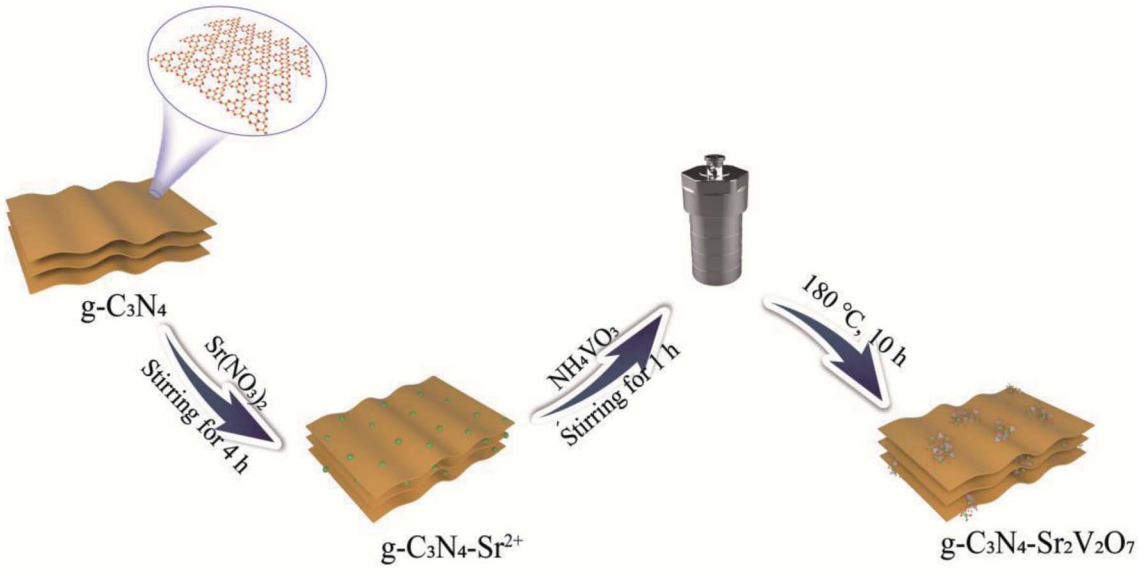

Scheme 1 Preparation process for the g-C_3N_4-$Sr_2V_2O_7$ nanohybrid.

Experimental

Synthesis of the g-C_3N_4-$Sr_2V_2O_7$

g-C_3N_4 (0.075 g) prepared by the reported method[16] was dispersed into DI water (140 mL). $Sr(NO_3)_2$ (10 mL, 0.01 mol L^{-1}) was slowly dropped into the g-C_3N_4 dispersion, and stirred for 4 h. Then the separated solid (g-C_3N_4-Sr^{2+}) was mixed with 70 mL DI water, and NH_4VO_3 (5 mL, 0.0132 mol L^{-1}) was put in and continuously reacted for another 1 h. After that, the mixture was put into a stainless Teflon-lined autoclave and heated at 180 °C for 10 h. It was naturally cooled to 25 °C. The solid (g-C_3N_4-$Sr_2V_2O_7$ nanohybrid) was washed thoroughly with DI water, and dried (Scheme 1).

Characterizations

Crystal structure of the samples was performed using Bruker D8 Advance X-ray diffractometer (XRD) equipped with Cu Kα irradiation (Germany). The interaction in materials were measured on a Thermo ESCALAB 250 X-ray photoelectron spectrometer (XPS) with a monochromatic X-ray source (Al Kα $h\nu = 1486.6$ eV) (USA). The light adsorption property was measured with a UV-3900 spectrophotometer (Japan). The morphology was observed by transmission electron microscopy (TEM, JEM-1400F, JEOL, Japan). The element maps were analyzed by a scanning electron microscope (SEM, S-3400N, Hitachi, Japan). The electron paramagnetic resonance (EPR) measurements were carried out on a Bruker ESP A300 spectrometer (Germany). The photoluminescence (PL) spectra were measured with an FL-4600 fluorescence spectrophotometer (Japan).

Photocatalytic measurement

Cr(VI) (with $K_2Cr_2O_7$ as Cr(VI) resource) reduction with the g-C_3N_4-$Sr_2V_2O_7$ nanohybrid as a photocatalyst was conducted in a quartz reactor under a 300 W xenon lamp. In order to reach the adsorption/desorption equilibrium, in each photocatalytic test, before irradiation, the mixture containing $K_2Cr_2O_7$ (represented by Cr(VI), 40 mL, 100 mg L^{-1}) aqueous solution and tartaric acid (30 mg) as well as g-C_3N_4-$Sr_2V_2O_7$ nanohybrid (10 mg) was stirred continuously for 1 h. During photocatalytic reaction, the residual Cr(VI) in the solution was monitored by a UV-vis spectrophotometer. Its concentration was obtained according to the absorbance of Cr(VI) at 540 nm and Lambert Beer's law.

Result and discussion

The characterization of the nanohybrid

XRD result of the as-prepared nanohybrid is displayed in Fig. 1A, a peak at 27.4° corresponds to (002) crystal plane of g-C_3N_4.[17] While the diffraction peaks appeared at $2\theta = 33.2°$ and 45.3° are originated from the (215) and (1012) planes of $Sr_2V_2O_7$, respectively (JCPDS No. 32-1268),[18] demonstrating that the $Sr_2V_2O_7$ is bound in the g-C_3N_4. In addition, the peaks of $Sr_2V_2O_7$ are weaker, which could be attributed to lower content (about 0.12 wt% measured by XPS), small size or high dispersion of $Sr_2V_2O_7$ in the nanohybrid. The morphology of the as-synthesized sample is studied by SEM and TEM. It shows some thicker sheet-like structures (Fig. 1B–D). The thickness of the blocky structure in SEM is about 0.92 μm measured by Digital Micrograph 3.9, and the thinner sheet-like structure is about 15.40 nm as observed in TEM image. Besides the sheet-like structure, no other morphology or crystal lattices are displayed. It is suggested that a small amount of $Sr_2V_2O_7$ is evenly distributed in the g-C_3N_4, which has little influence on the morphology of g-C_3N_4. The result is consistent with that in XRD. The $Sr_2V_2O_7$ in the sample is further identified by SEM mapping and XPS followed.

To further confirm the elemental distribution in the nanohybrid, the energy-filtered SEM image and elemental mappings

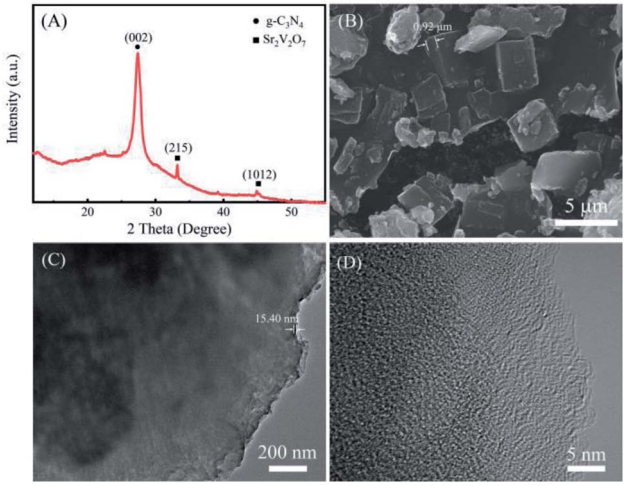

Fig. 1 The structure and morphology of the g-C_3N_4-$Sr_2V_2O_7$ nanohybrid. (A) XRD, (B) SEM, (C) TEM, (D) HRTEM.

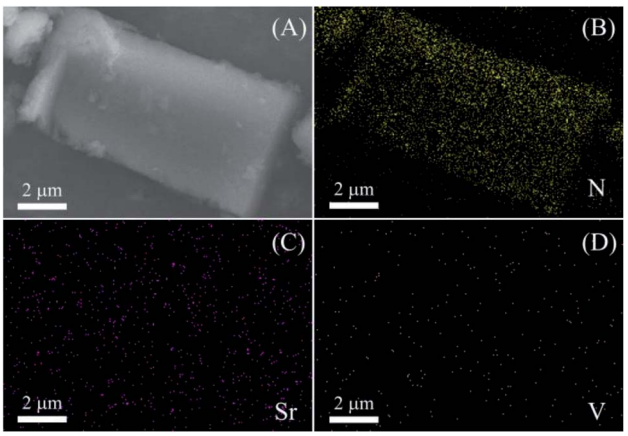

Fig. 2 (A) SEM image of the g-C_3N_4-$Sr_2V_2O_7$, (B) N map, (C) Sr map, and (D) V map.

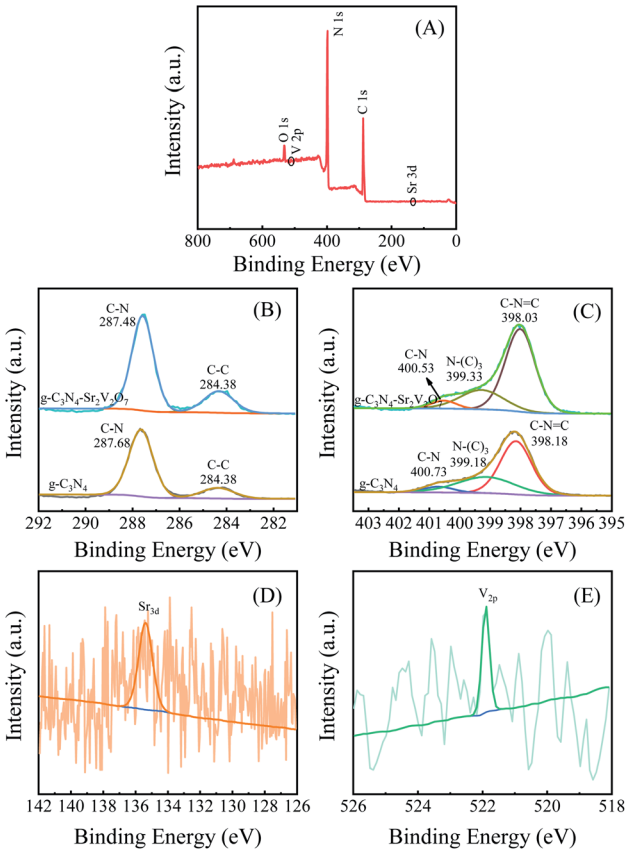

Fig. 3 (A) Survey XPS of the g-C_3N_4-$Sr_2V_2O_7$. The contrasting HRXPS of C 1s (B) and N 1s (C) in g-C_3N_4-$Sr_2V_2O_7$ and g-C_3N_4. The HRXPS of Sr 3d (D) and V 2p (E) in g-C_3N_4-$Sr_2V_2O_7$.

for the nanohybrid are taken. In Fig. 2, N, Sr and V can be observed in their mappings, which are matched with the theoretical composition of the obtained g-C_3N_4-$Sr_2V_2O_7$ nanohybrid. N element comes from g-C_3N_4, Sr and V elements come from the embedded $Sr_2V_2O_7$. Moreover, as displayed in Fig. 2C and D, the density of Sr and V is obviously lower than N, and the distribution of Sr and V mostly conforms to that of the N, indicating that the $Sr_2V_2O_7$ is relatively evenly implanted in the g-C_3N_4 hybrid.

According to the XPS shift in binding energy, the interaction among materials can be investigated. To confirm the interaction between $Sr_2V_2O_7$ and graphitic carbon nitride, XPS analysis is performed. In Fig. 3A, C, N, O, Sr and V elements in the g-C_3N_4-$Sr_2V_2O_7$ can be observed, which is consistent with those in Fig. 2. In C 1s spectrum of pristine g-C_3N_4 (Fig. 3B), the peaks at 287.68 and 284.38 eV are assigned to sp^2 hybridized carbon atom and the surface carbon, respectively.[19] The peak corresponding to C–N in the g-C_3N_4-$Sr_2V_2O_7$ is shifted toward lower binding energy relative to pristine g-C_3N_4. In Fig. 3C, the signals of N 1s in pristine g-C_3N_4 can be fitted into three peaks at 400.73, 399.18, and 398.18 eV, which are assigned to N–H, N–C_3, and C–N=C, respectively.[20] When $Sr_2V_2O_7$ is embedded into the graphitic carbon nitride, the peaks of C–N=C and N–H slightly shift towards lower binding energy, while the peak of the N–C_3 shifts towards higher energy, which are attributed to strong interaction between strontium vanadate and graphitic carbon nitride in the nanohybrid. However, the low signal-to-noise ratio of Sr and V spectra is observed in Fig. 3D and E, which could be attributed to the low content and lower sensitivity of Sr and V.

Photocatalytic Cr(VI) reduction

Performance of the prepared g-C_3N_4-$Sr_2V_2O_7$ nanohybrid is investigated by photocatalytic reduction of Cr(VI). Due to low content (only 0.12 wt%) of $Sr_2V_2O_7$ in the g-C_3N_4, its role in the composite photocatalyst is similar to a co-catalyst. Therefore, in photocatalytic measurement, the photocatalytic activity of the g-C_3N_4-$Sr_2V_2O_7$ nanohybrid was mainly compared with that of g-C_3N_4. Fig. 4A shows the time course of C/C_0 of Cr(VI) (C_0 and C are the concentrations of Cr(VI) at adsorption–desorption equilibrium and irradiated for t time, respectively). It is reported that tartaric acid can show photocatalytic activity for Cr(VI) reduction.[21] In this experiment, without any photocatalysts, only with tartaric acid, it needs about 13 min for complete

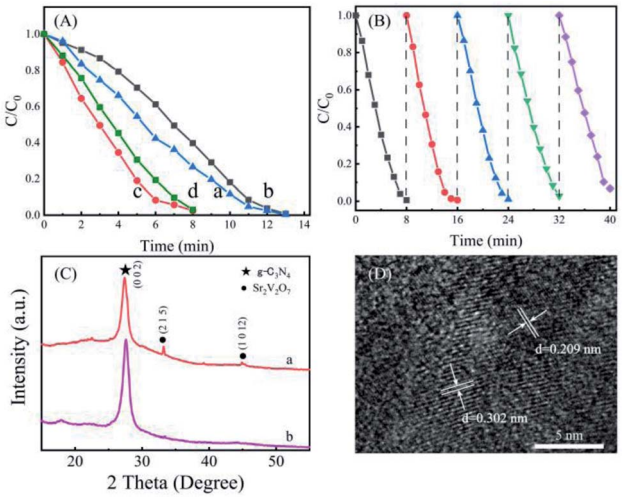

Fig. 4 (A) Time course of C/C_0 of Cr(VI) contained tartaric acid (a) without any photocatalysts, with (b) g-C_3N_4, with (c) g-C_3N_4-$Sr_2V_2O_7$ (0.12 wt%) nanohybrid, and with (d) g-C_3N_4-$Sr_2V_2O_7$ (0.06 wt%) nanohybrid; (B) photocatalytic recycling of the nanohybrid for Cr(VI) reduction; (C) the XRD patterns of the g-C_3N_4-$Sr_2V_2O_7$ nanohybrid before recycling experiment (a) and after recycling experiment (b); (D) HRTEM image of the g-C_3N_4-$Sr_2V_2O_7$ nanohybrid after recycling experiment.

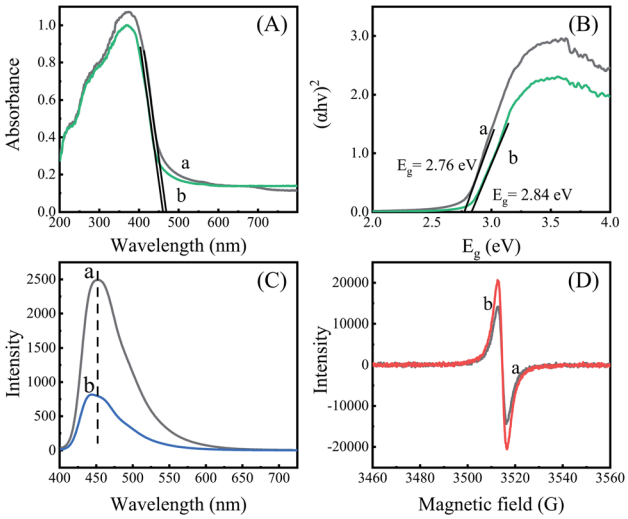

Fig. 5 (A) Solid diffuse reflectance spectra; (B) Tauc plots; (C) fluorescence spectra, λ_{ex} = 380 nm; (D) EPR spectra. (a) g-C_3N_4, (b) g-C_3N_4-$Sr_2V_2O_7$.

reduction of Cr(VI). However, after pure g-C_3N_4 was introduced in the solution, its photocatalytic rate is lower than that only with tartaric acid, especially in the first ten minutes. Surprisingly, after the g-C_3N_4-$Sr_2V_2O_7$ is added, under same conditions, 100% Cr(VI) was quickly reduced within 8 min. The reduction time of Cr(VI) is decreased about 5 min compared with that of pure g-C_3N_4. When the content of $Sr_2V_2O_7$ is decreased from 0.12 wt% to 0.06 wt%, as shown in Fig. 4A(d), photocatalytic activity of nanohybrid is decreased. However, it is still higher than that of pure g-C_3N_4. It is indicated that the photocatalytic performance of graphitic carbon nitride can be effectively improved by embedded strontium vanadate.

A good photocatalyst, besides its activity, its stability is also an important parameter that needs to be considered in practical applications. Therefore, as an active photocatalyst for Cr(VI) removal, the reusability of the g-C_3N_4-$Sr_2V_2O_7$ hybrid is evaluated by five successive recycling tests. In the experiment, after the first photocatalytic reaction, the solution was removed by centrifugation, and the fresh Cr(VI) solution (100 mg L^{-1}, 40 mL) was added for the next cycle. As displayed in Fig. 4B, after 5 recycles, the photocatalytic performance of the nanohybrid is changed little, and almost 100% Cr(VI) is reduced in each recycle. TEM and powder XRD after recycling experiment were measured. As shown in Fig. 4C and D, after recycling experiment, the intensity of diffraction peaks of $Sr_2V_2O_7$ in the nanohybrid is decreased. It is deduced that some $Sr_2V_2O_7$ fall off the nanohybrid during recycling. In the TEM image of the g-C_3N_4-$Sr_2V_2O_7$ nanohybrid after recycling experiment, some crystal planes ((1012), (215)) corresponding to $Sr_2V_2O_7$ are shown, which cannot be observed in TEM image of the nanohybrid before recycling experiment (Fig. 1D). It is indicated that some $Sr_2V_2O_7$ particles grow up, and the crystallinity is improved during recycling. The two aspects are opposite to the photocatalytic activity. Subsequently, the photocatalytic activity of nanohybrid changes little after five recycling. The result demonstrates that the g-C_3N_4-$Sr_2V_2O_7$ nanohybrid *in situ*

Table 1 Performance of some common photocatalysts for Cr(VI) reduction

References	Materials	Dosage of catalyst (mg mL^{-1})	The concentration of Cr(VI) (mg L^{-1})	Time (min) and efficiency (%)	Light source
Ref. 22	TiO_2/CN/rGO	0.5	100	240 min, 97%	300 W Xe lamp
Ref. 23	Biochar-g-C_3N_4 microspheres	40	50	240 min, 100%	300 W Xe lamp
Ref. 24	Br-doped g-C_3N_4	1	20	120 min, 62%	300 W Xe lamp
Ref. 10	(P,Mo)-CN	1.25	100	120 min, 95%	300 W Xe lamp
Ref. 25	$CaFe_2O_4$/g-C_3N_4/CNT	1	10	120 min, 97%	300 W Xe lamp
Ref. 26	CNT@MoS_2/SnS_2	1	50	90 min, 100%	300 W Xe lamp
Ref. 11	P-CN/SnS	0.5	100	60 min, 100%	300 W Xe lamp
Ref. 27	γ-CD/MoS_2/g-C_3N_4	0.4	10	50 min, 81%	300 W Xe lamp
Ref. 28	g-C_3N_4@bio-Fe(III)-hydroxysulfate	0.2	20	20 min, 100%	300 W Xe lamp
In this paper	g-C_3N_4-$Sr_2V_2O_7$	0.25	100	8 min, 99%	300 W Xe lamp

prepared by hydrothermal method is with relatively higher stability, and is an effective and potential material for photocatalytic Cr(VI) removal.

For photocatalytic reduction of Cr(VI), many materials can be used as photocatalysts. As shown in Table 1, using the g-C_3N_4-$Sr_2V_2O_7$ hybrid as the photocatalyst, in a shorter time (8 min), Cr(VI) reduction can be completed. Moreover, the Cr(VI) with higher concentration can be reduced by less dosage of the g-C_3N_4-$Sr_2V_2O_7$ nanohybrid. It further demonstrates that the hybrid is a more active photocatalyst for Cr(VI) removal.

To explore the reason for the improved photocatalytic performance in the g-C_3N_4-$Sr_2V_2O_7$, the light adsorption property of the samples is studied. Clearly, in Fig. 5A, the g-C_3N_4 shows an absorption edge at *ca.* 468 nm. The corresponding band gap is 2.76 eV (Fig. 5B), which is in agreement with the reported result.[29] And the nanohybrid displays comparable light-absorption, absorption edge is at 459 nm, and the corresponding band gap is 2.84 eV, showing that light adsorption and band gap of graphitic carbon nitride is changed little by the incorporation of $Sr_2V_2O_7$.

In addition, fluorescence spectra are measured in order to explore charge separation in the nanohybrid. Generally, a higher emission indicates more e^-/h^+ recombination and poorer photocatalytic performance.[30] It can be seen in Fig. 5C, g-C_3N_4 shows a high emission at 453 nm, while the g-C_3N_4-$Sr_2V_2O_7$ exhibits a weaker emission. Besides, an about 9 nm blue-shift is seen in the emission spectrum of the nanohybrid, suggesting that the embedding of strontium vanadate in the graphitic carbon nitride plays an important role in inhibiting recombination of e^-/h^+ pairs due to strong interaction between strontium vanadate and graphitic carbon nitride. It is very advantageous to increase photocatalytic performance of the g-C_3N_4-$Sr_2V_2O_7$ nanohybrid.

To better substantiate and comprehend the charge separation in the nanohybrid, the EPR measurements are performed. In Fig. 5D, only one single Lorentzian line at $g = 2.003$ is shown for the two samples. It is ascribed to nitrogen vacancies.[31] In the nanohybrid, the EPR signal is increased compared with that of the graphitic carbon nitride, suggesting more nitrogen vacancies generated in the nanohybrid. According to the results in Fig. 5, it is concluded that more nitrogen vacancies generated in the g-C_3N_4-$Sr_2V_2O_7$ could be the intrinsic reason for increased charge separation and photocatalytic performance in the nanohybrid.

Conclusions

g-C_3N_4-$Sr_2V_2O_7$ nanohybrid was smartly *in situ* synthesized by hydrothermal method. The nanohybrid with intimate contact showed fast and highly efficient removal of Cr(VI). Moreover, its photocatalytic performance was hardly changed after five successive recycling tests. The lower fluorescence and increased EPR signals achieved in the nanohybrid evidenced that highly efficient charge separation originated from more nitrogen vacancies in the nanohybrid was the main reason for the increased photocatalytic performance in the g-C_3N_4-$Sr_2V_2O_7$. The work will provide an idea for designing a greatly preferable and recyclable photocatalyst for the removal of other heavy metal ions in wastewater.

Conflicts of interest

There are no conflicts to declare.

Acknowledgements

This work was financially supported by National Natural Science Foundation of China (No. 21771125, 21301118 and 21305092).

References

1 V. E. Pakade, N. T. Tavengwa and L. M. Madikizela, *RSC Adv.*, 2019, **9**, 26142–26164.
2 S.-S. Wu, W.-C. Hou and D. K. Wang, *Environ. Sci.: Nano*, 2020, **7**, 2399–2409.
3 C. Yang, T. Ju, X. Wang, Y. Ji, C. Yang, H. Lv, Y. Wang, W. Dong, F. Dang, X. Shi, W. Wang and Y. Fan, *RSC Adv.*, 2020, **10**, 10612–10623.
4 S. M. El-Sheikh, A. B. Azzam, R. A. Geioushy, F. M. El Dars and B. A. Salah, *J. Alloys Compd.*, 2020, **13**, 157513–157524.
5 P. Zhou, X. Meng, L. Li and T. Sun, *J. Alloys Compd.*, 2020, **827**, 154259–154265.
6 X. Bai, Y. Li, L. Xie, X. Liu, S. Zhan and W. Hu, *Environ. Sci.: Nano*, 2019, **6**, 2850–2862.
7 L. Zhao, Z. Zhao, Y. Li, X. Chu, Z. Li, Y. Qu, L. Bai and L. Jing, *Nanoscale*, 2020, **12**, 10010–10018.
8 K. Wang, Y. Li, J. Li and G. Zhang, *Appl. Catal., B*, 2020, **263**, 117730–117739.
9 J. Lin, J. Hu, C. Qiu, H. Huang, L. Chen, Y. Xie, Z. Zhang, H. Lin and X. Wang, *Catal. Sci. Technol.*, 2019, **9**, 336–346.
10 D. Chen, J. Liu, Z. Jia, J. Fang, F. Yang, Y. Tang, K. Wu, Z. Liu and Z. Fang, *J. Hazard. Mater.*, 2019, **361**, 294–304.
11 H. Sun and S.-J. Park, *Appl. Surf. Sci.*, 2020, **531**, 147325.
12 C. Yang, Z. Xue, J. Qin, M. Sawangphruk, S. Rajendran, X. Zhang and R. Liu, *J. Phys. Chem. C*, 2019, **123**, 4795–4804.
13 G. Zhan, W. C. Ng, S. N. Koh and C.-H. Wang, *ACS Sustainable Chem. Eng.*, 2018, **6**, 2292–2301.
14 A. Sharma, M. Varshney, K.-H. Chae and S. O. Won, *RSC Adv.*, 2018, **8**, 26423–26431.
15 S. Zhan, F. Zhou, N. Huang, Y. Yin, M. Wang, Y. Yang and Y. Liu, *J. Mol. Catal. A: Chem.*, 2015, **401**, 41–47.
16 X. Zhao, Y. Zhang, X. Zhao, X. Wang, Y. Zhao, H. Tan, H. Zhu, W. Ho, H. Sun and Y. Li, *ACS Appl. Mater. Interfaces*, 2019, **11**, 27934–27943.
17 B. Li, Q. Fang, Y. Si, T. Huang, W.-Q. Huang, W. Hu, A. Pan, X. Fan and G.-F. Huang, *Chem. Eng. J.*, 2020, **397**, 125470–125482.
18 S. K. Gupta, K. Sudarshan and R. M. Kadam, *Mater. Des.*, 2017, **130**, 208–214.
19 K. Wang, L. Jiang, X. Wu and G. Zhang, *J. Mater. Chem. A*, 2020, **8**, 13241–13247.
20 H. Hu, J. Hu, X. Wang, J. Gan, M. Su, W. Ye, W. Zhang, X. Ma and H. Wang, *Catal. Sci. Technol.*, 2020, **10**, 4712–4725.

21 Z. Xu, Y. Yu, D. Fang, J. Liang and L. Zhou, *Mater. Chem. Phys.*, 2016, **171**, 386–393.
22 G. Li, Y. Wu, M. Zhang, B. Chu, W. Huang, M. Fan, L. Dong and B. Li, *Ind. Eng. Chem. Res.*, 2019, **58**, 8979–8989.
23 Q. Jin, G. Xie, X. Cai, X. Hu, H. Wang, G. Qiu, W. Wang, D. Zhou, H. Huo, X. Tan and Y. Zhao, *RSC Adv.*, 2020, **10**, 6121–6128.
24 M. Wang, Y. Zeng, G. Dong and C. Wang, *Chin. J. Catal.*, 2020, **41**, 1498–1510.
25 F. Liu, S. Dong, Z. Zhang, X. Li, X. Dai, Y. Xin, X. Wang, K. Liu, Z. Yuan and Z. Zheng, *RSC Adv.*, 2019, **9**, 25750–25761.
26 J. Wan, P. Xue, R. Wang, L. Liu, E. Liu, X. Bai, J. Fan and X. Hu, *Appl. Surf. Sci.*, 2019, **483**, 677–687.
27 Z. Wu, X. He, Y. Xue, X. Yang, Y. Li, Q. Li and B. Yu, *Chem. Eng. J.*, 2020, **399**, 125747–125758.
28 X. Wang, Y. Xie, X. Chen, X. Zhou, W. Hu, P. Li, Y. Li, Y. Zhang and Y. Wang, *Chem. Eng. J.*, 2020, **398**, 125632–125644.
29 X. Wu, H. Ma, W. Zhong, J. Fan and H. Yu, *Appl. Catal., B*, 2020, **271**, 118899–118906.
30 M. Zhou, G. Dong, F. Yu and Y. Huang, *Appl. Catal., B*, 2019, **256**, 117825–117835.
31 X. a. Dong, J. Li, Q. Xing, Y. Zhou, H. Huang and F. Dong, *Appl. Catal., B*, 2018, **232**, 69–76.